JOURNAL OF RHEOLOGY

Using startup of steady shear flow in a sliding plate rheometer to determine material parameters for the purpose of predicting long fiber orientation

Kevin Ortman, Donald Baird, Peter Wapperom, and Abby Whittington

Citation: Journal of Rheology (1978-present) **56**, 955 (2012); doi: 10.1122/1.4717496
View online: http://dx.doi.org/10.1122/1.4717496
View Table of Contents: http://scitation.aip.org/content/sor/journal/jor2/56/4?ver=pdfcov
Published by the The Society of Rheology

Using startup of steady shear flow in a sliding plate rheometer to determine material parameters for the purpose of predicting long fiber orientation

Kevin Ortman and Donald Baird[a)]

Chemical Engineering, Virginia Tech, Blacksburg, Virginia 24061

Peter Wapperom

Mathematics, Virginia Tech, Blacksburg, Virginia 24061

Abby Whittington

Material Science and Engineering, Virginia Tech, Blacksburg, Virginia 24061

(Received 1 August 2011; final revision received 20 March 2012; published 21 May 2012)

Synopsis

The properties of long glass fiber reinforced parts, such as those manufactured by means of injection molding and compression molding, are highly dependent on the fiber orientation generated during processing. A sliding plate rheometer was used to understand the transient stress and orientation development of concentrated long glass fibers during the startup of steady shear flow. An orientation model and stress tensor combination, based on semiflexible fibers, was assessed in its ability to predict fiber orientation when using model parameters obtained from the fits of the stress responses. Specifically, samples of different initial fiber orientations was subjected to the startup of steady shear flow, and an orientation model based on bead and rod theory was coupled with a derived stress tensor that accounts for the semiflexibility of the fibers to obtain the corresponding model parameters. The results showed the semiflexible orientation model and stress tensor combination, overall, provided improved rheological results as compared to the Folgar–Tucker model when coupled with the stress tensor of Lipscomb *et al*. [J. Non-Newtonian Fluid Mech. **26**, 297–325 (1988)]. Furthermore, it was found that both stress tensors required empirical modification to accurately fit the measured data. Finally, orientation models provided encouraging results when predicting the transient fiber orientation for all initial fiber orientations explored. © *2012 The Society of Rheology*. [http://dx.doi.org/10.1122/1.4717496]

I. INTRODUCTION

The phrase "long fiber" is used in this context to describe fibers that are able to bend or flex during flow and thus during processing. This bending and flexing, in general, can affect both the material's microstructure and properties. Subsequently, the term "flexibility" will be used to describe the fiber's tendency to bend in the presence of flow.

[a)]Author to whom correspondence should be addressed; electronic mail: dbaird@ut.edu

Specifically, a fiber exhibiting a larger degree of flexibility is easier to bend within a specified flow field. Switzer and Klingenberg (2003) quantified the effective stiffness (S^{eff}) of a fiber in a viscous medium by proposing a dimensionless group that contains both the viscosity of the matrix, the fiber aspect ratio ($a_r = L/d$, where L is the fiber length and d is the diameter) and the Young's modulus (E_Y) of the fiber

$$S^{eff} = \frac{E_Y \pi}{64 \eta_m \dot{\gamma} a_r^4}. \tag{1}$$

In Eq. (1), η_m is the matrix viscosity and $\dot{\gamma}$ is the shear rate. From this expression, the stiffness of a fiber can be seen to decrease (increased flexibility) with aspect ratio for a given material (i.e., fixed Young's modulus). For the case of glass, fibers less than 1 mm in length are often considered to be "short" (and hence rigid) while fibers of length greater than 1 mm are considered to be "long" (and hence flexible). This length is somewhat arbitrary but is related to the influence of fiber length on the mechanical properties of the solid composite, see, for example, Crosby (1991).

Predicting the transient rheological response of long fiber suspensions is complex because of various factors such as fiber-matrix and fiber-fiber interactions. These factors become more prominent in high concentration regimes, where the volume fraction of fibers, ϕ, is $\geq a_r^{-1}$ [Doi and Edwards (1988)]. This is because as fiber concentration is increased, short range hydrodynamic forces, frictional, and other mechanical interactions between the fibers also increase. To study these interactions and understand fiber orientation from a fundamental approach, direct simulations of individual fibers have been used. In such simulations, model fiber equations are usually constructed for a single or small population of fibers and consist of the equations of forces and torques that evolve the particles and fiber configurations over time. Many authors use direct simulations to try and explore phenomena believed to be of interest, such as long and short range hydrodynamic effects, flexibility, Coulombic forces, and frictional forces, for example, see the work of Yamamoto and Matsuoka (1993, 1995), Skjetne *et al.* (1997), and Joung *et al.* (2001). Direct simulations, however, are currently very limited in their application to real processing flows due to the high computational resources needed to use them.

Keshtkar *et al.* (2009) were one of the first groups to study the effect of flexibility on the transient shear rheology of fiber suspensions. They studied the start-up and flow reversal rheology of fibers with different flexibilities in a Newtonian oil using a parallel disk rheometer. They found an increase in both the start-up viscosity and first normal stress difference with increased flexibility and also a delayed response in flow reversal. Later, Keshtkar *et al.* (2010) also began a quantitative analysis of the transient fiber orientation. Experimentally, they found fibers with increased flexibility orientated more slowly than rigid fibers. In this work, they used rheological data to obtain orientation material parameters for an orientation and a stress model combination based on the GENERIC framework of Rajabian *et al.* (2005). This model, applicable for nondilute suspensions, was constructed to supply a mesoscopic level of information pertaining to the fiber microstructure evolution and the resulting stresses within the suspension. This model has the advantage of supplying consistency between the flow dynamics equations and thermodynamics. Simulation results showed that the viscosity could be fitted reasonably well, but obtained relatively poor performance in fitting the normal stress difference. On comparison between the model's predicted transient orientation and experimentally measured values, they found that the model parameters obtained from the rheology only qualitatively represented the transient orientation.

The conventional way of handling fiber orientation stems from short fiber theory wherein the orientation of a rigid fiber can be described as a vector that is parallel to the fiber, denoted in Fig. 1 as **p**. For a given orientation distribution function ψ, wherein ψ describes the probability of finding a fiber of specific orientation within an θ, φ, and $\theta + \mathrm{d}\theta$, $\varphi + \mathrm{d}\varphi$, the second moment of ψ may be evaluated in the following way to form an orientation tensor (**A**), as presented in the works of Advani and Tucker (1987).

$$\mathbf{A}(t) = \int \mathbf{pp}\psi(\mathbf{p}, t)d\mathbf{p}. \tag{2}$$

The orientation tensor provides a convenient means of describing the orientation of a population of fibers. For example, if the fibers are all oriented in the 1-direction (i.e., the flow direction), the orientation tensor will have an A_{11} component of 1.0, and 0 for all other components. Likewise, an initial 3-direction orientation would have an orientation tensor, whose A_{33} component is 1.0, and 0 for all other components. Consequently, fibers randomly oriented in the 1–3 plane will have components $A_{11} = A_{33} = 0.5$, with 0 for all other components.

Originally, Jeffery (1922) derived an expression describing the motion of an ellipsoidal particle in a flow field. In a continuum sense, Jeffery's model is

$$\frac{D\mathbf{A}}{Dt} = \mathbf{W} \cdot \mathbf{A} - \mathbf{A} \cdot \mathbf{W} + \xi(\mathbf{D} \cdot \mathbf{A} + \mathbf{A} \cdot \mathbf{D} - 2\mathbf{D} : \mathbf{A}_4), \tag{3}$$

wherein $\mathbf{W} = [(\nabla \mathrm{v})^{\mathrm{t}} - \nabla \mathrm{v}]/2$ is the vorticity tensor, $\mathbf{D} = [(\nabla \mathrm{v})^{\mathrm{t}} + \nabla \mathrm{v}]/2$ is the rate of strain tensor, and ξ is a shape factor defined in terms of the particles aspect ratio as $\xi = (a_r^2 - 1)/(a_r^2 + 1)$ as has been presented in the work of Advani and Tucker (1987). In this context, the velocity gradient is defined as $\nabla \mathrm{v}_{\mathrm{ij}} = \partial \mathrm{v}_{\mathrm{j}}/\partial \mathrm{x}_{\mathrm{i}}$. The fourth order

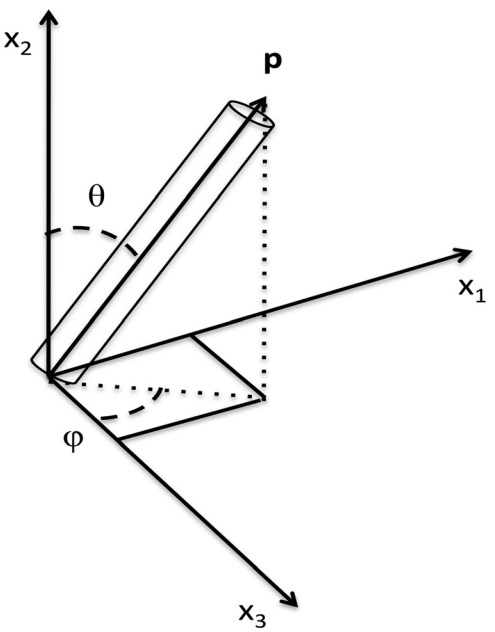

FIG. 1. Rigid fiber with orientation vector **p**.

orientation tensor is defined as the fourth moment of the orientation distribution function as given

$$\mathbf{A}_4(t) = \int \mathbf{pppp}\psi(\mathbf{p}, t)d\mathbf{p}. \tag{4}$$

$\mathbf{A}_4$ requires a closure approximation to decouple this fourth order tensor in terms of the second order orientation tensor $\mathbf{A}$. Common forms of this closure approximation are expressed through linear, quadratic, hybrid, and higher order polynomial closures such as the invariant-based optimal fitting (IBOF) approximation, Chung and Kwon (2001). As the aspect ratio of the ellipsoid becomes larger, the period of orbital dynamics becomes much longer. If the aspect ratio is forced to be infinitely large, as has been used to approximate the aspect ratio of fibers, ξ approaches unity and the period of rotation becomes infinite and allows this particle to asymptotically orient with the flow field. In retrospect, it can be seen that Jeffery's model provides a way of describing the motion of a rigid, mass-less, fiber in an infinitely dilute suspension. All dynamics are purely hydrodynamic (no fiber interactions), but this model provided a starting point for exploring more realistic dynamics such as fiber interactions.

Folgar and Tucker (1984) hypothesized in nondilute suspensions that fiber interactions could be captured by an isotropic rotary diffusion term which is added to Jeffery's model as shown

$$\frac{D\mathbf{A}}{Dt} = \mathbf{W}\cdot\mathbf{A} - \mathbf{A}\cdot\mathbf{W} + \xi(\mathbf{D}\cdot\mathbf{A} + \mathbf{A}\cdot\mathbf{D} - 2\mathbf{D}:\mathbf{A}_4) + 2C_I\dot{\gamma}(\mathbf{I} - 3\mathbf{A}), \tag{5}$$

where C_I is the isotropic rotary diffusion coefficient and $\mathbf{I}$ is the identity tensor, and $\dot{\gamma} = (2\mathbf{D}:\mathbf{D})^{1/2}$ is the scalar magnitude of $\mathbf{D}$. Much researches have been conducted with Eq. (5), but this model in many cases over predicts the rate of fiber orientation and, in general, was found to describe the orientation of short fibers only qualitatively well, such as shown in the work of Bay (1991) and Eberle *et al.* (2010). In a later paper, Eq. (5) was modified to incorporate a method that allowed for the slowing of the orientation dynamics and is referred to as the reduced strain closure (RSC) model [Wang *et al.* (2008)]. The RSC model is much more complex as compared to Eq. (5), and instead a simpler method has been proposed in the past by Huynh (2001) by incorporating a slip coefficient (α) to be multiplied by the right hand side of Eq. (5) to form

$$\frac{D\mathbf{A}}{Dt} = \alpha(\mathbf{W}\cdot\mathbf{A} - \mathbf{A}\cdot\mathbf{W} + \xi(\mathbf{D}\cdot\mathbf{A} + \mathbf{A}\cdot\mathbf{D} - 2\mathbf{D}:\mathbf{A}_4) + 2C_I\dot{\gamma}(\mathbf{I} - 3\mathbf{A})). \tag{6}$$

In Eq. (6), α is a number between 0 and 1 and reduces the rate of fiber orientation. Adding the slip coefficient to the Folgar–Tucker equation results in a loss of material objectivity, for example, see the work of Wang *et al.* (2008), but the behavior of the model is still valid in the case of simple shear flow, as shown by Eberle *et al.* (2010). Additionally, an anisotropic rotary diffusion (ARD) form of the Folgar–Tucker equation exists, but will not be discussed in this research, and instead the reader is referred to the work of Phelps and Tucker (2009).

A continuum model that accounts for the orientation evolution of semiflexible fibers is that proposed by Strautins and Latz (2007) and is referred to here as the Bead–Rod model. In this model, a semiflexible fiber is modeled as two connected "rods" of orientation $\mathbf{p}$ and $\mathbf{q}$, each of length l_B that may flex about a central pivot point, as shown in Fig. 2. The semiflexible fiber has a resistance to bending and is accounted for by a

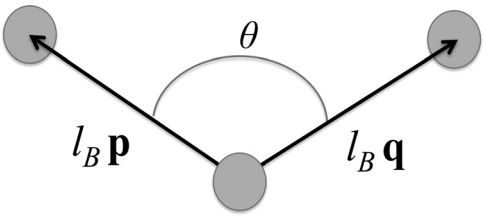

FIG. 2. Semiflexible (bead and rod) fiber model of Strautins and Latz (2007). Fiber is constructed by two connected orientation vectors **p** and **q**.

resistance potential that exists between both rods. When the fiber is perfectly straight no restorative force exists within the fiber. However, if the fiber is placed in a flow that may induce fiber curvature, the fiber bends in response to the drag flow on the "beads."

To model the orientation changes of such fibers, Strautins and Latz (2007) developed the kinematic equations for the bead and rod fiber in Fig. 2. Several assumptions were made. First, this model applies for fibers that are only semiflexible for which $\mathbf{p} \approx -\mathbf{q}$. The exact extent to this restriction, however, was not fully described. Second, similar to Jeffrey's equation, the model fiber is assumed to be in an infinitely dilute suspension where only hydrodynamic effects may exist and does not allow for interactions between different fibers. The model describes the evolution of Eq. (3) moments of the **p** and **q** vectors in the following manner:

$$\mathbf{A}(t) = \int\int \mathbf{pp}\,\psi(\mathbf{p},\mathbf{q},t)d\mathbf{p}d\mathbf{q}, \tag{7}$$

$$\mathbf{B}(t) = \int\int \mathbf{pq}\,\psi(\mathbf{p},\mathbf{q},t)d\mathbf{p}d\mathbf{q}\,, \tag{8}$$

$$\mathbf{C}(t) = \int\int \mathbf{p}\,\psi(\mathbf{p},\mathbf{q},t)d\mathbf{p}d\mathbf{q}, \tag{9}$$

Equation (7) is similar to what exists in rigid rod theory [Eq. (2)] and describes the second moment of any one of the rods with respect to the orientation distribution function. Another orientation tensor describes the mixed product of both rod vectors with the orientation distribution function, Eq. (8). Finally, the first moment of the distribution function, using either rod's orientation vector, Eq. (9) is also formed. It is important to note that this single moment, Eq. (9), does not always vanish in the case of the Bead–Rod model as it does for a purely rigid rod model. The equations describing the evolution of these moments are given

$$\begin{aligned}\frac{D\mathbf{A}}{Dt} &= (\mathbf{W}\cdot\mathbf{A} - \mathbf{A}\cdot\mathbf{W}) + (\mathbf{D}\cdot\mathbf{A} + \mathbf{A}\cdot\mathbf{D} - 2\mathbf{D}:\mathbf{A}_4)\\ &\quad + \frac{l_B}{2}[\mathbf{Cm} + \mathbf{mC} - 2(\mathbf{m}\cdot\mathbf{C})\mathbf{A}] - 2k[\mathbf{B} - \mathbf{A}\ \mathrm{tr}(\mathbf{B})],\end{aligned} \tag{10}$$

$$\begin{aligned}\frac{D\mathbf{B}}{Dt} &= (\mathbf{W}\cdot\mathbf{B} - \mathbf{B}\cdot\mathbf{W}) + (\mathbf{D}\cdot\mathbf{B} + \mathbf{B}\cdot\mathbf{D} - (2\mathbf{D}:\mathbf{A})\mathbf{B})\\ &\quad + \frac{l_B}{2}[\mathbf{Cm} + \mathbf{mC} - 2(\mathbf{m}\cdot\mathbf{C})\mathbf{B}] - 2k[\mathbf{A} - \mathbf{B}\ \mathrm{tr}(\mathbf{B})],\end{aligned} \tag{11}$$

$$\frac{D\mathbf{C}}{Dt} = \nabla\boldsymbol{v}^t\cdot\mathbf{C} - (\mathbf{A}:\nabla\boldsymbol{v}^t)\,\mathbf{C} + \frac{l_B}{2}[\mathbf{m} - \mathbf{C}\,(\mathbf{m}\cdot\mathbf{C})] - k\,\mathbf{C}[1 - \mathrm{tr}(\mathbf{B})]\,, \tag{12}$$

$$\mathbf{m} = \sum_{i=1}^{3}\sum_{j=1}^{3}\sum_{k=1}^{3}\frac{\partial^2 v_i}{\partial x_j \partial x_k} A_{jk}\,\mathbf{e}_i. \tag{13}$$

Within these equations, *tr*() represents the trace of a specified tensor and k is the resistive bending potential coefficient. Physically, as the value of k increases, the Bead–Rod model behaves more like a rigid fiber, and in the limit as k approaches infinity, reproduces Jeffery's model [Eq. (3)] for high aspect ratio particles. Conversely, as k approaches 0, the fiber behaves more flexibly. In these equations, flexibility is induced only by hydrodynamic effects, as quantified by the second order spatial derivatives of the velocity term that exists in Eq. (13). Within Eq. (13), $\mathbf{m}$ is a vector formed by the summation over the indices *ijk*, and $\boldsymbol{e}_i$ are the directional unit vectors.

To predict the stress response of a fiber suspension, a stress tensor is also needed (in combination with an orientation model). Most of the works pertaining to the understanding of stress theory for fiber suspensions can be traced back to Ericksen (1960), Batchelor (1971), Goddard (1978), Dinh and Armstrong (1984), Shaqfeh and Fredrickson (1990), and Gibson and Toll (1999). In general, researchers often look for a form of a stress equation such that the total stress ($\boldsymbol{\sigma}$) on the suspension is a linear combination of stresses contributed by the suspending medium and the stresses contributed by the particles as

$$\boldsymbol{\sigma} = -P\mathbf{I} + \tau_{\text{Matrix}} + \tau_{\text{Particles}}. \tag{14}$$

In Eq. (14), P is the isotropic pressure, $\boldsymbol{\tau}_{\text{Matrix}}$ is the stress contribution from the matrix. Equivalently, $\boldsymbol{\tau}_{\text{Matrix}}$ may be replaced with $\boldsymbol{\tau}_{\text{Matrix}} = 2\eta_{\text{m}}\,\mathbf{D}$. The most general form for the viscous stress tensor for a suspension of rigid, nonconcentrated, ellipsoid particles is

$$\boldsymbol{\sigma} = -P\mathbf{I} + 2\eta_m\mathbf{D} + 2\eta_m\phi\{a\mathbf{A}_4 : \mathbf{D} + b(\mathbf{D}\cdot\mathbf{A} + \mathbf{A}\cdot\mathbf{D}) + c\mathbf{D} + f\mathbf{A}D_r\}, \tag{15}$$

wherein a, b, c, and f are geometric shape factors and D_r is the rotary diffusivity due to Brownian motion. For high aspect ratio particles, such as fibers, $b = 0$. For glass fibers (long and short), Brownian motion is negligible and so D_r may considered to be negligible. This reduces Eq. (15) to the form suggested by Lipscomb *et al.* (1988) for high aspect ratio particles as

$$\boldsymbol{\sigma} = -P\mathbf{I} + 2\eta_m(\mathbf{D} + c\phi\mathbf{D} + N\mathbf{A}_4 : \mathbf{D}). \tag{16}$$

In Eq. (16), N is a function of the fiber concentration and aspect ratio and c is a parameter attributed to a stress enhancement caused by the presence of a volume fraction of fibers. For completeness, in the case where $c = 0$, the stress theory of both Ericksen (1960) and Hand (1962) is presented. We will, however, retain the stress tensor written in Eq. (16) for this research. Much works have gone into analytically determining the values of c and N in the dilute through semidilute regimes, see, for example, the work of Lipscomb *et al.* (1988). No theory, however, exists for fiber systems that are concentrated and some authors have chosen not to use analytical expressions for c and N, but rather have chosen to use them as a fitting parameter, such as in the work of Eberle *et al.* (2009). Additionally, strictly speaking, no stress theory to date considers fibers that are flexible. Finally, the fourth order orientation tensor appears in Eq. (16) and may be accompanied by the use of a closure approximation.

Combining this stress expression with the Folgar–Tucker orientation model previously discussed has yielded varying degrees of success depending on the concentration level. For example, in the work of Eberle *et al.* (2010), rheological measurements for

concentrated short fiber suspensions were modeled using the Folgar–Tucker model and the stress tensor in Eq. (16). Their results yielded shear stress and normal stress difference values that could not be fit in either the magnitude or peak breadth. This performance is due to a general lack of understanding of concentrated fiber interactions and is especially suspected when fiber flexibility is a non-negligible variable. No other studies seem to exist in which the transient rheology of concentrated fiber suspensions (short or long) is studied to obtain necessary modeling parameters.

In this research, we use a sliding plate rheometer to explore the behavior of long glass fibers (LGFs) in simple shear flow. The sliding plate is chosen instead of conventional rotational rheometers due to the deficiencies associated with their measurement of fiber suspensions. Specifically, rotational devices such as parallel disk rheometers are known to cause inhomogeneous fiber orientation development, due to the inhomogeneous shear field between the disks, and the results in superficially enhanced stress measurements and longer stress responses than would exist if the shear field was homogenous, as shown by Eberle *et al*. (2009). A cone-and-disk with bored out center is the more appropriate choice for short fiber suspensions but still is unable to provide a large enough gap for LGFs. Hence, the sliding plate rheometer provides unique and useful benefits for measuring long fiber suspensions, because it provides a homogenous shear field and may be constructed to give gaps of various thicknesses, as demonstrated by Giacomin *et al*. (1989).

The purpose of this paper was to determine if Bead–Rod theory, when coupled with a stress tensor that accounts for flexibility, could be used to fit the rheological responses of LGF suspensions. We used rigid fiber theory (Folgar–Tucker model coupled with the Libscomb stress model) as a basis for performance comparison. Finally, we wished to assess the performance of the parameters (obtained from the rheological fits) in their ability to predict the transient fiber orientation, with the hopes of later using these parameters to predict fiber orientation in more complex flows such as those found in injection molding.

II. THEORY

In this section, we discuss modifications made to extend the Bead–Rod theory to nondilute suspensions. Next, we derive an appropriate stress contribution due to the semiflexible nature of the Bead–Rod model. Finally, we suggest empirical modifications, to the stress theory, that are needed to obtain better performance at fitting the rheological response of long fiber suspensions.

A. Bead-rod modifications

As derived, the Bead–Rod model is theoretically only applicable to dilute semiflexible fiber suspensions. Consequently, in an attempt to extend this model for the purpose of exploring nondilute suspensions, such as those of commercial interest, we considered that the isotropic rotary diffusion term, suggested by Folgar and Tucker (1984), be added to the Bead–Rod model. The Bead–Rod model, now applicable for nondilute suspensions, is given as

$$\frac{D\mathbf{A}}{Dt} = \alpha\Bigg((\mathbf{W}\cdot\mathbf{A}-\mathbf{A}\cdot\mathbf{W}) + (\mathbf{D}\cdot\mathbf{A}+\mathbf{A}\cdot\mathbf{D}-2\mathbf{D}:\mathbf{A}_4) - 6C_I\dot{\gamma}\left(\mathbf{A}-\frac{1}{3}\mathbf{I}\right) + \frac{l_B}{2}[\mathbf{Cm}+\mathbf{mC}-2(\mathbf{m}\cdot\mathbf{C})\mathbf{A}] - 2k[\mathbf{B}-\mathbf{A}\ \mathrm{tr}(\mathbf{B})]\Bigg), \tag{17}$$

$$\frac{D\mathbf{B}}{Dt} = \alpha((\mathbf{W}\cdot\mathbf{B} - \mathbf{B}\cdot\mathbf{W}) + (\mathbf{D}\cdot\mathbf{B} + \mathbf{B}\cdot\mathbf{D} - (2\mathbf{D}:\mathbf{A})\mathbf{B}) - 4C_I\dot{\gamma}\,\mathbf{B} + \frac{l_B}{2}[\mathbf{C}\mathbf{m} + \mathbf{m}\mathbf{C} - 2(\mathbf{m}\cdot\mathbf{C})\mathbf{B}] - 2k[\mathbf{A} - \mathbf{B}\ \mathrm{tr}(\mathbf{B})]\Big), \tag{18}$$

$$\frac{D\mathbf{C}}{Dt} = \alpha\left(\nabla\boldsymbol{v}^t\cdot\mathbf{C} - (\mathbf{A}:\nabla\boldsymbol{v}^t)\,\mathbf{C} + \frac{l_B}{2}[\mathbf{m} - \mathbf{C}\,(\mathbf{m}\cdot\mathbf{C})] - k\,\mathbf{C}[1 - \mathrm{tr}(\mathbf{B})] - 2C_I\dot{\gamma}\,\mathbf{C}\right), \tag{19}$$

$$\mathbf{m} = \sum_{i=1}^{3}\sum_{j=1}^{3}\sum_{k=1}^{3}\frac{\partial^2 v_{\mathrm{i}}}{\partial x_{\mathrm{j}}\partial x_{\mathrm{k}}}A_{\mathrm{jk}}\,\mathbf{e}_{\mathrm{i}}. \tag{20}$$

Each term containing C_I in Eqs. (17)–(19) is the associated isotropic rotary diffusion term as it applies to the Bead–Rod model. The derivation of these terms can be found in the Appendix A. Additionally, α has been added to each of the above equations and retains the identical meaning, as it does when used with the Folgar–Tucker model, Eq. (6). In this form, flexibility may be exhibited not only by the fluid velocity field [Eq. (20)] but also by fiber-fiber interactions accounted through rotary diffusion. For example, in the work of Strautins and Latz (2007), they mathematically demonstrated the case of a semiflexible fiber in the presence of a parabolic (channel) flow and showed the flow field was able to bend the fiber due to the presence of second order derivatives of the velocity field [i.e., Eq. (20)]. With the addition of the isotropic rotary diffusion term [terms containing C_I in Eqs. (17)–(19)], bending may also be mathematically introduced phenomenologically by fiber-fiber interactions. This source of bending may be thought of as a rotary diffusion induced bending. Physically, this exists because each fiber segment may interact with other fibers. Mathematically, the isotropic rotary diffusion term drives the orientation of the fibers to a random state, such as in the Folgar–Tucker model. The same phenomenon occurs with the Bead–Rod model, but in addition to randomizing orientation, the bending angle of this semiflexible model is also driven to a random state. This is a unique consequence of the semiflexible model. Hence, two sources of bending, in general, exist for the modified Bead–Rod model.

B. Bending stress addition

A bending stress may be derived from the bending potential function of the Bead–Rod model and is added to Eq. (16), see Appendix B for the derivation. This contribution to the suspension stress is caused by an average nonzero bending angle of the fibers with a restorative potential coefficient, k. In this case of the Bead–Rod model, the total stress tensor of the suspension becomes

$$\boldsymbol{\sigma}_{\mathrm{BR}} = \boldsymbol{\sigma} + \eta_m k\frac{3\phi a_r}{2}(\mathbf{B} - \mathbf{A}\,tr(\mathbf{B})). \tag{21}$$

Equation (21) can be written in terms of a tensor, $\mathbf{r}$, derived from the second moment of the end-to-end vector of the Bead–Rod fiber. In this manner, Eq. (21) becomes

$$\boldsymbol{\sigma}_{\mathrm{BR}} = \boldsymbol{\sigma} + \eta_m k\frac{3\phi a_r}{2}\frac{tr(\mathbf{r})}{2l_B^2}(\mathbf{A} - \mathbf{R}), \tag{22}$$

where the dimensional end-to-end orientation tensor, $\mathbf{r}$, is defined as the second moment of the end-to-end vector, $l_B(\mathbf{p} - \mathbf{q})$, with respect to ψ in Eq. (23). Upon full evaluation,

Eq. (23) simplifies to Eq. (24). Additionally, **R** may be defined as a normalized and dimensionless form of **r** as in Eq. (25).

$$\mathbf{r} \equiv \int\int l_B^2(\mathbf{p}-\mathbf{q})\,(\mathbf{p}-\mathbf{q})\psi(\mathbf{p},\mathbf{q},t)d\mathbf{p}d\mathbf{q}, \tag{23}$$

$$\mathbf{r} = 2l_B^2(\mathbf{A}-\mathbf{B})\,, \tag{24}$$

$$\mathbf{R} \equiv \frac{\mathbf{r}}{tr(\mathbf{r})} = \frac{\mathbf{A}-\mathbf{B}}{1-tr(\mathbf{B})}. \tag{25}$$

As can be seen in Eq. (22), when $\mathbf{R}=\mathbf{A}$, corresponding to a perfectly straight fiber system ($\mathbf{q}=-\mathbf{p}$), the bending stress term drops out and the original stress equation for a rigid fiber is regained, Eq. (16). This occurs in the absence of bending when the flexible fiber is perfectly straight or behaves like a rigid rod. On the other hand, when the fiber does exhibit bending, the bending stress term is not zero and is a function of both the end-to-end distance, as quantified by $tr(\mathbf{r})$, and the difference between the **A** and **R** orientation tensors, Eq. (22). To elaborate, the root-mean squared end-to-end distance of the population of fibers is simply equal to the square root of $tr(\mathbf{r})$. Thus, for the special case of a population of straight fibers (wherein $\mathbf{q}=-\mathbf{p}$ and hence $\mathbf{B}=-\mathbf{A}$), the root-mean squared end-to-end distance is simply $2l_B$, which is equal to the summed length of both fiber legs (see Fig. 2). In general, this distance will be reduced by the degree of bending within the fibers ($<2l_B$) and **R** will differ from **A**. For semiflexible fibers (small bending angles), the values of the components of these two orientation tensors will always be similar, however. Like **A**, the $tr(\mathbf{R})=tr(\mathbf{A})=1$ and **R** is symmetric. Equations (24) and (25), in combination with Eq. (22), provide a means for calculating the total stress contribution of the fiber suspension, including effects due to the semiflexibility of the fibers.

C. Empirical modifications to the stress tensor

In this research, we considered empirical modifications to the stress tensor. Specifically, we propose empirically modifying the Lipscomb model [Eq. (16)] by weighting each term by a function rather than a constant, as shown in the following equations:

$$\boldsymbol{\sigma}_{\text{mod}} = -P\mathbf{I} + 2\eta_m(\mathbf{D} + f_1\phi\mathbf{D} + f_2\mathbf{A}_4 : \mathbf{D}), \tag{26}$$

$$f_1 = \begin{cases} \frac{c_1}{\dot{\gamma}_{\min}^b} & \text{for} \quad \dot{\gamma} \le \dot{\gamma}_{\min} \\ \frac{c_1}{\dot{\gamma}^b} & \text{for} \quad \dot{\gamma} > \dot{\gamma}_{\min} \end{cases}, \tag{27}$$

$$f_2 = c_2\, I_{\mathbf{A}} II_{\mathbf{A}} III_{\mathbf{A}}, \tag{28}$$

where

$$I_{\mathbf{A}} = tr(\mathbf{A}) = 1, \tag{29}$$

$$II_{\mathbf{A}} = \frac{1}{2}\left[tr(\mathbf{A})^2 - tr(\mathbf{AA})\right], \tag{30}$$

$$III_{\mathbf{A}} = \det(\mathbf{A}). \tag{31}$$

The purpose of these modifications [Eqs. (27) and (28)] is to aid in the fitting of the overshoot magnitude and steady-state stress values, Eqs. (27) and (28), respectively, which otherwise would yield poor results if constant weights were used [such as Eq. (16) or (22)]. Such difficulty in using the conventional Lipscomb stress model, in combination with the Folgar–Tucker model, to fit the experimentally observed overshoot, for example, has been reported by Eberle *et al*. (2009). In their work, the Lipscomb model did not predict any stress overshoot when using experimentally consistent initial fiber orientation conditions, even though one existed experimentally. To avoid this difficulty, an empirical modification is suggested, f_2, whose value [Eq. (28)] is the product of the invariants of $\mathbf{A}$, as defined in Eqs. (29)–(31), and is scaled by a fitting parameter c_2. The purpose of this term is to aid in capturing large stress overshoots experimentally observed, which would otherwise be very difficult to describe with its original form, i.e., Eq. (16). The invariants were chosen as weighting functions because they represent scalar quantities that are dependent solely on the orientation state of the system and additionally are not affected by the choice of coordinate system. It is believed that other functions involving the invariants of $\mathbf{A}$ may also be of use. Equation (28) represents a simple choice for the purpose of exploring such an empirical modification. A second empirical modification, f_1, is also suggested. The purpose of f_1 [Eq. (27)] in practice is to fit experimentally observed shear thinning in excess of that exhibited from just the polymer matrix. More specifically, the value of the weighting function f_1 is largest at low $\dot{\gamma}$ and decreases with increasing $\dot{\gamma}$ and mathematically allows for a reduction in the steady-state stress contribution from the volume fraction term in Eq. (26), which has been observed experimentally by Ortman *et al*. (2011). Without this modification, experimentally observed steady shear stress values would be restricted to only vary with the shear rate dependence of the neat matrix, and not necessarily with the suspension. In this function, b is a fitted exponent that quantifies how the value of f_1 changes with $\dot{\gamma}$, and c_1 is a linear fitting parameter. One obtains the conventional Lipscomb's form of this term by setting $b=0$. To prohibit f_1 from becoming infinite at very low rates of strains, a restraint is enforced below a minimum $\dot{\gamma}(\dot{\gamma}_{\min})$ such that f_1 becomes constant. For example, $\dot{\gamma}_{\min}$ can simply be equated to the lowest $\dot{\gamma}$ employed in the measurements. Again, f_1 and f_2 are examples of empirical adaptations believed needed to more accurately match the experimentally measured rheological responses of our long fiber suspensions. An example of fitting rheological data with and without the suggested empirical modifications [Eqs. (27) and (28)], in combination with the Folgar–Tucker model, will be shown in Sec. IV. Finally, the Bead–Rod stress tensor was modified in an identical manner and yields the following form:

$$\boldsymbol{\sigma}_{\mathrm{BR-mod}} = -P\mathbf{I} + 2\eta_m(\mathbf{D} + f_1\phi\mathbf{D} + f_2\mathbf{A}_4 : \mathbf{D}) + \eta_m k\frac{3\phi a_r}{2}\frac{tr(\mathbf{r})}{2l_B^2}(\mathbf{A} - \mathbf{R}). \tag{32}$$

III. EXPERIMENTAL AND COMPUTATIONAL METHODS

A. Materials and preparation

The LGF reinforced polypropylene material was provided by SABIC Innovative Plastics and had an initial concentration of 30 wt. % ($\phi = 0.145$). The material was extruded to provide fiber mixing and erase the thermal history of the matrix. The initial fiber pellets of length of 13 mm was reduced significantly during the extrusion process, and it was found via digital imaging that the materials had an average fiber length (L_N) of 2.92 mm. The average diameter of the fibers was $d = 14.5$ μm. The extrudate was collected and pelletized into long strands to be compression molded for rheological testing. An additional

concentration of 10 wt. % ($\phi = 0.048$) material was prepared in the same manner. In all cases, the glass fiber systems used in this research possessed a ϕ such that, using the theory of Doi and Edwards (1988), the suspensions were classified as concentrated, $\phi \geq a_r^{-1}$.

LGF samples were prepared having three different prescribed initial fiber orientations. The sample material was made by extruding, collecting, and cutting the fiber material into strands. These strands were then manually placed in a rectangular mold with preferential orientation. The orientation was confirmed using digital imaging, as discussed in Sec. III B. These samples were initially oriented either in the flow direction (x_1 direction), the neutral direction (x_3-direction), or random in the plane (x_1-x_3 plane) with respect to the coordinate system in Fig. 3, and will be referred to as D1, D3, and DX samples, respectively. The D1 samples were prepared by laying 76 mm strands parallel to each other in the flow direction of a 254 mm × 76 mm mold, and then were compression molded at 180 °C for 15 min. Rheological tests were performed on the neat matrix to verify its integrity after being heated for this length of time, and no signs of degradation were observed. Similarly, D3 samples were prepared by laying 76 mm strands in the neutral direction of the mold. The samples having fibers oriented randomly in the 1–3 plane (DX) were fabricated by randomly distributing 15 mm strands of the extruded strands in the mold and then compression molding them. Two different lengths of extruded strands (76 and 15 mm) were used to achieve the intended initial orientations more accurately. Specifically, the DX samples required a smaller length strand to achieve better homogeneity and random orientation. All the samples prepared had final dimensions of 254 mm × 76 mm × 1.70 mm. However, the thickness varied between 1.65 and 1.85 mm. All samples were prepared and experimented with at 180 °C.

B. Measurement of fiber orientations

Fiber orientation of the sheared samples was measured using a micrographic technique proposed by Hine *et al*. (1996). In this method, a solidified sample is cut and carefully polished to expose the elliptical cross-sections of the intersecting fibers within the polymer sample. The phrase "elliptical cross-section" refers to a fiber in a polished plane intersection that is captured on a micrograph. This cross-section is quantitatively analyzed to determine the projection of the fiber, and hence the orientation for a population of fibers. Samples were polished using alumina oxide based polishing grits and slurries. A polished sample length of three times the average fiber diameter was imaged using an optical microscope along the full part thickness. Specifically, each sample taken was 10 mm × 1.5 mm. A digital imaging program was written to analyze the cross-sectional ellipses to determine the values of the orientation tensor. The results shown in this research depict the average of three independent samples. Within each polished sample, at least 1000 fibers for each 10 wt. % sample and 3000 fibers for each 30 wt. % sample were analyzed over the polished sample dimensions.

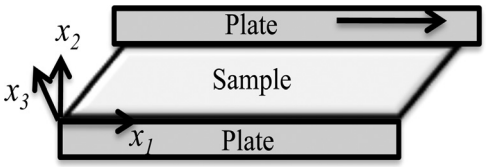

FIG. 3. Sliding plate rheometer and defined coordinate system, Ortman *et al*. (2011).

C. Sliding plate rheometer

The sliding plate rheometer used in this work was fabricated based on the design initially developed by Giacomin *et al.* (1989). The apparatus was encased in a forced convection oven (Russells Technical Products, Model RB-2-340) and was mounted vertically in an electromagnetic drive system, specifically an Instron-4204. The Instron can be programmed to drive the moving plate at a desired speed (limited to a plate velocity of approximately 450 mm/min and total shearing displacement of 200 mm). Once the plate is set into motion, the melt sample therein is sheared homogeneously. The resulting shear stress is measured using a shear stress transducer (SST) that is flush mounted to the stationary plate. The rigid lever in the SST, suspended by a diaphragm, deflects in response to the applied stress of the moving fluid. It causes the other end of the lever to deflect in the opposite direction. This deflection is measured using a capacitance probe, Capacitec, Model HPT-75G-E-L2-2-B-D. The signals from the probe are amplified in a signal amplifier (Capacitec 4100-SL-BNC Amplifier Card) and then sent to a data acquisition card (National Instruments USB-6008). The device has been calibrated to convert and quantify the resulting deflection into a shear stress. The calibration was performed using a fluid of known viscosity. A detailed discussion of the calibration procedure adopted for the constructed device can be found elsewhere, for example, in the work of Koran and Dealy (1999) and Agarwal (2009). Two different diaphragms were constructed with different sensitivities to allow a range of materials to be tested in the SPR. The gap between the stationary and moving plate of the SPR was kept at 1.50 mm and yields a gap to fiber diameter ratio of approximately 100 for all glass systems analyzed. This ratio is above the ratio used for short glass fiber samples, as proposed in the work of Sepehr *et al.* (2004) and Eberle *et al.* (2010). The effect of gap on LGF samples, however, has not yet been determined. Samples were squeezed down to the rheometer gap (1.50 mm) during the insertion process and allowed better wall-matrix contact before they were sheared. In all rheological experiments conducted within this research, at least three samples were tested per experiment. Reported results are an average of the samples tested and have an average standard deviation $<15\%$ for the 10 wt. % fiber samples, and $<20\%$ for the 30 wt. % fiber samples. Additionally, each sample's deformed length was measured after shearing and compared to the programmed Instron displacement. In all cases, less than $\pm 3\%$ discrepancy exists between repeated runs, and this suggests slippage between the sample and plates is negligible.

D. Physical property values

This section discusses our choice for handling the physical property values of l_B, k, and η_m. Two model variables, both l_B and k, are present in the Bead–Rod model and are related to physical characteristics of the fibers. First, l_B is defined as the half length of a fiber. In the case of our samples, a population of fiber lengths exists. Hence, to describe the population of fibers with one l_B value, we have chosen to use the number average l_B associated with our fiber length distribution. Hence, this length scale simply becomes $l_B = L_N/2$ or $l_B = 1.46$ mm. Likewise, we need to associate a single k value to the population of fibers. To do this, we chose to calculate the number average k value over the fiber length distribution, where n_i is the number of fibers associated with each k_i, in the following manner:

$$k = \frac{\sum_i n_i k_i}{\sum_i n_i}. \tag{33}$$

As a reminder, k is the bending potential (energy) coefficient associated with the internal rigidity of a fiber. In physical terms, we have chosen to associate this term with the bending potential of a beam under small deflection. This allowed us to determine the value of k using the physical properties of the fibers. An expression for k can be obtained by equating the potential energy of a beam under deflection with the potential energy expression for the bead and rod fiber. Please refer to Strautins and Latz (2007) concerning the expression of the Bead–Rod energy expression. Additionally, one would need to equate the magnitude of force on the hypothetical beam with the magnitude of the sum of the internal restorative vector forces from the rods of the fiber, wherein the beam (fiber) is in static equilibrium. Once accomplished, the expression can be algebraically solved for k and approximated in the limit as $\mathbf{q}$ approaches $-\mathbf{p}$ (semiflexible approximation). Finally, expressions for the second moment of inertia for the hypothetical beam and coefficient of drag on a sphere in Stokes' flow may be inputted, and an expression for k is obtained. For a population of fiber lengths, each k_i is found to be a function of E_Y, d, η_{m}, and the l_B of each fiber in the population (l_{Bi}). In these terms, k_i becomes

$$k_i = \left(\frac{E_Y}{64\,\eta_m}\right)\frac{d^3}{l_{Bi}^3}. \tag{34}$$

Assuming $E_Y = 80$ GPa and $\eta_{\mathrm{m}} = 560$ Pa s, then after using Eqs. (34) and (33) in combination with our fiber length distribution, $k = 218\ \mathrm{s}^{-1}$. As k approaches infinity it becomes stiffer, and as it approaches 0 it becomes perfectly flexible. Our value will demonstrate itself to be only semiflexible within our rheological experiments.

Finally, for the purpose of the stress tensors used in this research, the experimentally measured matrix viscosity was calculated at each shear rate and inputted for η_m within the stress equations [Eqs. (26) and (32)]. This eliminated the need to fit a generalized Newtonian model to the matrix viscosity.

E. Parameter fitting and numerical methods

The major goal of this work was to obtain a unique set of rheological model parameters for a given material (i.e., fiber length, concentration, and matrix properties) and then assess the accuracy of the models in their abilities to predict the transient fiber orientation. Although being able to model the rheology is important, the most important aspect is the ability to predict the evolution of fiber orientation and then eventually translate this information to be useful with general (complex) flow situations. To obtain these model parameters, we chose to best fit our models to the DX samples (i.e., samples with an initial random fiber orientation) for both the 10 wt. % and 30 wt. % materials.

The method for obtaining the parameters is outlined in Fig. 4. The initial orientation for our samples was measured, using the method described in Sec. III B, and numerically specified for each simulation. As Fig. 4 shows, the orientation and stress model parameters are initially guessed. Next, the orientation equations are solved, and the stress equation is calculated and numerically compared to rheological data. The difference between the calculated stress and the rheologically measured stress, or residual difference, is squared and summed. Next, stress parameters values are iterated on to find a local minimum residual difference. Once accomplished, orientation model parameters are then again revisited to try to obtain an even lower residual difference. This process is continued several times until the best fit is obtained. A commercial

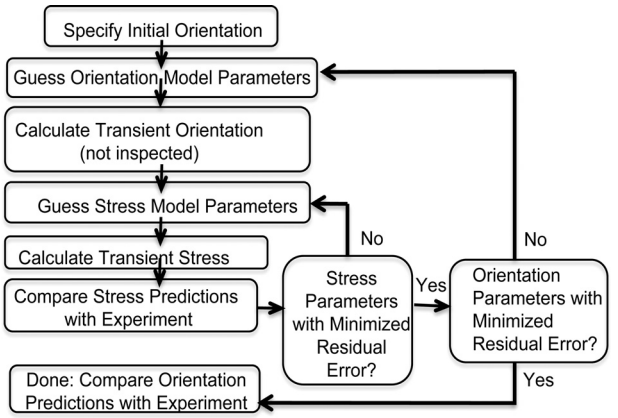

FIG. 4. Method for determining material parameters from rheological data.

solver (MATHEMATICA) was used to solve the initial value, differential orientation equations.

F. Closure approximations

A closure approximation was used to decouple the fourth order orientation tensor $\mathbf{A}_4$ in terms of the second order orientation tensor $\mathbf{A}$. In this research, we used the 5th degree polynomial IBOF closure approximation both in the Folgar–Tucker model and in the Bead–Rod model, Eq. (17). The reader is referred to the work of Chung and Kwon (2001) for a description of the IBOF closure approximation. It will be stated, for completion, that during the derivation of the Bead–Rod model higher mixed moments of both $\mathbf{p}$ and $\mathbf{q}$ naturally arose. These moments too required closure, and Strautins and Latz (2007) listed criteria that should be met to provide such closures. In the end, Strautins and Latz suggested a closure relationship similar to the quadratic closure, see, for example, Advani and Tucker (1990), to be used within Eqs. (18) and (19). Their closure was used in this work as they suggested in Eqs. (18) and (19).

G. Initial conditions

Samples were prepared with various initial fiber orientations (DX, D3, and D1), and this initial orientation was measured using the method discussed in Sec. III B. For a given initial arrangement, the initial orientations only differed slightly between samples with different fiber concentrations. This difference was within experimental error. Hence, for each initial fiber arrangement (DX, D3, and D1), the same initial orientation conditions were used for both 10 wt. % and 30 wt. % samples. Additionally, because we are interested in a two-dimensional (2D) simulation of the fiber orientation and assuming isotropy in the neutral direction (x_3), the off-diagonal orientation components in the neutral direction were set to 0 (i.e., $A_{i3,\ i\neq 3}=0$, and $A_{3i,\ i\neq 3}=0$). The significance of this assumption implies that our sample microstructures possessed no out-of-plane preference in the neutral direction. For the simple shear flow experiments in this research, we have experimental evidence that suggests this assumption is actually quite good; otherwise, this work would have required additional experimental considerations, needed to accurately measure these components, other than those discussed in this text. The reader, for example, is referred to the work of Vélez-García *et al.* (2011) for such a discussion. The initial measured orientation for each fiber arrangement is listed below

$$\mathbf{A}(0) = \overset{\text{DX}}{\begin{pmatrix} 0.565 & 0.037 & 0 \\ 0.037 & 0.038 & 0 \\ 0 & 0 & 0.397 \end{pmatrix}}, \quad \mathbf{A}(0) = \overset{\text{D3}}{\begin{pmatrix} 0.093 & 0.065 & 0 \\ 0.065 & 0.080 & 0 \\ 0 & 0 & 0.827 \end{pmatrix}},$$
$$\mathbf{A}(0) = \overset{\text{D1}}{\begin{pmatrix} 0.863 & 0.025 & 0 \\ 0.025 & 0.043 & 0 \\ 0 & 0 & 0.094 \end{pmatrix}}. \tag{35}$$

For the Bead–Rod model, other initial conditions were needed for Eqs. (18) and (19). As of now, fiber curvature cannot be measured, so we have chosen to assume that the fibers are initially straight before each experiment, and hence, $\mathbf{B}(0) = -\mathbf{A}(0)$, and $\mathbf{C}(0) = \mathbf{0}$.

IV. SIMULATION RESULTS AND DISCUSSION

In this section, we discuss the performance of the stress models' ability to match the transient rheology obtained with the sliding plate rheometer. A discussion of the rheological behavior itself, however, has already been provided by Ortman *et al*. (2011) and for brevity will not be reproduced here. We will also discuss the ability of the models to predict fiber orientation for a variety of different initial fiber orientations and shear rates.

A. 30 wt. % materials

Modeling parameters for all the materials were determined using the transient viscosity (shear) data obtained for the DX samples (at each concentration) and are listed in Table I. To summarize the model parameters α, C_I, c_1, b, c_2, and were obtained from the rheology, and k (specific to the Bead–Rod model) was determined from fiber material properties and fiber length distribution as described in Sec. III D. For the semiflexible fiber predictions, a combination of the Bead–Rod model [Eqs. (17)–(20)] and its

TABLE I. Model parameters determined from rheological fits for both the 30 and 10 wt. % materials. For completion, k is recorded but is not fit from the rheology and is instead determined in the manner discussed in Sec. III D.

30 wt. %	Folgar–Tucker	Bead–Rod
C_I	5.0×10^{-3}	5.3×10^{-2}
α	0.25	0.13
c_1	15	24
b	1.0	0.65
c_2	5.2×10^5	1.4×10^5
k	N/A	218 s^{-1}
10 wt. %	Folgar–Tucker	Bead–Rod
C_I	3.5×10^{-3}	4.0×10^{-2}
α	0.32	0.27
c_1	1.5	5
b	2.2	1.4
c_2	3.1×10^5	1.1×10^5
k	N/A	218 s^{-1}

corresponding stress model Eq. (32) was used and will be referred to as the BR-$\sigma_{\text{BR-mod}}$ combination. For the rigid fiber predictions, a combination of the Folgar–Tucker model [Eq. (6)] and the modified Lipscomb stress tensor [Eq. (26)] was used and will be referred to as the FT- σ_{mod} combination.

As can be seen in Fig. 5, the BR-$\sigma_{\text{BR-mod}}$ combination does a better job at fitting the transient viscosity values for the 30% DX samples at all shear rates than does the FT-σ_{mod}. Specifically, the BR-$\sigma_{\text{BR-mod}}$ combination provides a much better representation of the experimentally measured stress overshoot. The necessity for stress tensor modifications may also be seen in this situation. For this example, one will notice in Fig. 5 that when using the Folgar–Tucker and conventional Lipscomb stress tensor [Eq. (16)] without modification (FT-σ), very poor performance is obtained comparably, especially in its ability to capture the stress overshoot. This lack of ability to capture the stress response is what prompted the modifications discussed in Sec. II C. When the empirically modified stress is used (i.e., FT-σ_{mod}), however, the model performs much better. In addition, when using the BR-$\sigma_{\text{BR-mod}}$ combination it was found that the magnitude of the bending stress accounts for several percent reductions in the total stress contribution, Eq. (32), as was the case at 1.0 s^{-1}. The degree of bending may be calculated from the root-mean-squared end-to-end distance using tr(**r**), see Sec. II B and Eq. (24). Although the degree of bending is not graphically shown here, it was found that the k value in the Bead–Rod model for the current fiber suspension corresponded only to a very slight degree of bending (reduction in the end-to-end distance $\ll 1\%$). This magnitude of fiber bending, though very small, was found to increase fairly linearly with shear rate. This bending is directly due to competing forces between the internal rigidity of the fiber and isotropic rotary diffusion. But, again, the degree of bending was very small in all cases even for the current semiflexible system. This is because, in the case of our glass fiber system, bending induced from isotropic rotary diffusion is much smaller than the internal rigidity of the fibers and contributes to a very small change to the degree of fiber bending. This bending, as stated before, however, was shown to alter the stress response by several percents and signifies that even small degrees in bending can result in non-negligible stress effects. Another consequence to the rotary diffusion induced bending was that the Bead–Rod model required larger C_I values to obtain similar behavior as the Folgar–Tucker model, even at sufficiently rigid k values. Consequently, when using the rotary diffusion term within the Bead–Rod model, this simply means a larger range of C_I values will be needed as compared to that used with the Folgar–Tucker model. Note, it was found that for both the Bead–Rod model and the Folgar–Tucker model, $C_I > 0$ and $\alpha < 1$ were required to

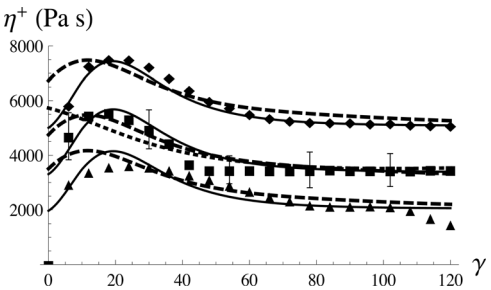

FIG. 5. Viscosity vs strain data for the 30 wt. % initially planar random oriented samples measured at 0.4 s^{-1} (◆), 1.0 s^{-1} (■), and 4.0 s^{-1} (▲). Also, fit of the Bead–Rod model and the (modified/proposed) stress tensor [Eq. (32)] combination (solid plot), and fit of the Folgar–Tucker model and (modified) stress tensor [Eq. (26)] combination (dashed plot). Finally, for reference, a fit of the Folgar–Tucker model and (conventional Lipscomb) stress tensor [Eq. (16)] (dotted plot) at 1.0 s^{-1}. Error bars denote the experimental standard deviation of the data.

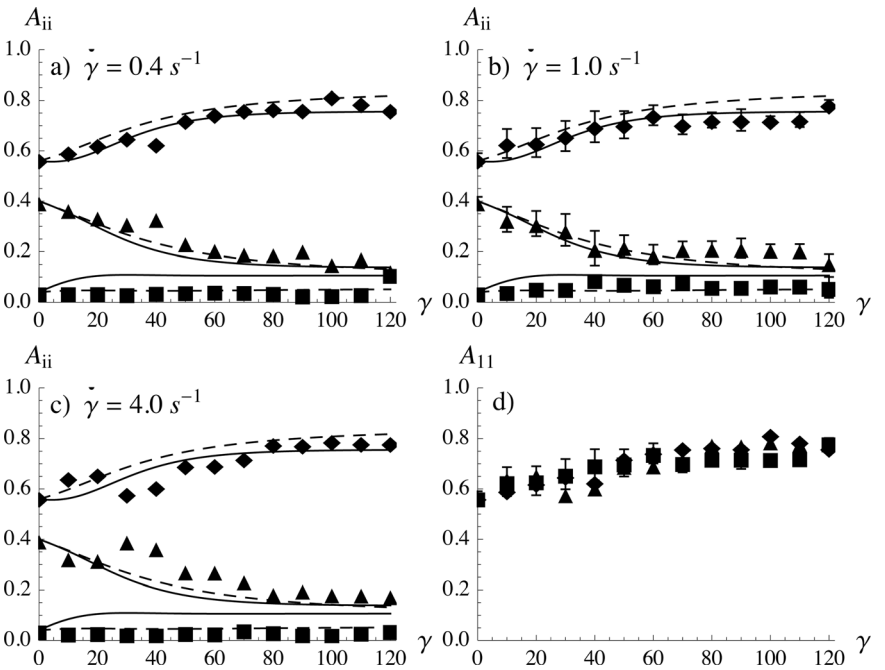

FIG. 6. Comparison of orientation vs strain predictions of the Bead–Rod (solid plot) and Folgar–Tucker (dashed plot) models with experimental orientation data A_{11} (◆), A_{22} (■), and A_{33} (▲) for 30 wt. % initially planar random oriented samples sheared at all shear rates, (a) 0.4 s^{-1}, (b), 1.0 s^{-1}, (c) 4.0 s^{-1}. (d) Comparison of experimental data A_{11} vs strain for 0.4 s^{-1} (◆), 1.0 s^{-1} (■), and 4.0 s^{-1} (▲). Error bars denote the standard deviation of the data.

best fit the transient viscosity (η^+). The significance of this remains in that both C_I and α are necessary to best fit the rheology.

Now that all the model parameters have been determined for the 30 wt. % material (Table I), it is of interest to see how the models' predictions of the orientation compare with experimentally measured values. As can be seen in Figs. 6(a)–6(c), the overall performance of both models is encouraging. In the case of both orientation models, good accuracy in matching both the rise and steady-state values of the A_{11} and A_{33} orientation components is met. Additionally, the Bead–Rod model offers slight improvement in

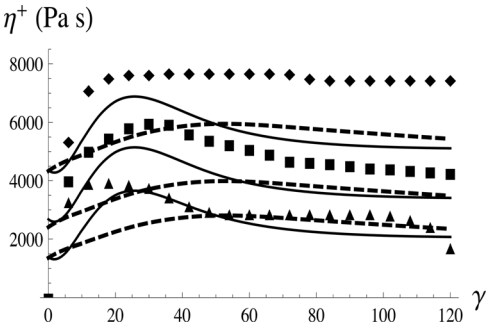

FIG. 7. Viscosity vs strain data for the 30 wt. % initially neutral-direction oriented samples measured at 0.4 s^{-1} (◆), 1.0 s^{-1} (■), and 4.0 s^{-1} (▲). Also, fit of the Bead–Rod model and (modified/proposed) stress tensor [Eq. (32)] combination (solid plot), and fit of the Folgar–Tucker model and (modified plot) stress tensor [Eq. (26)] combination (dashed plot).

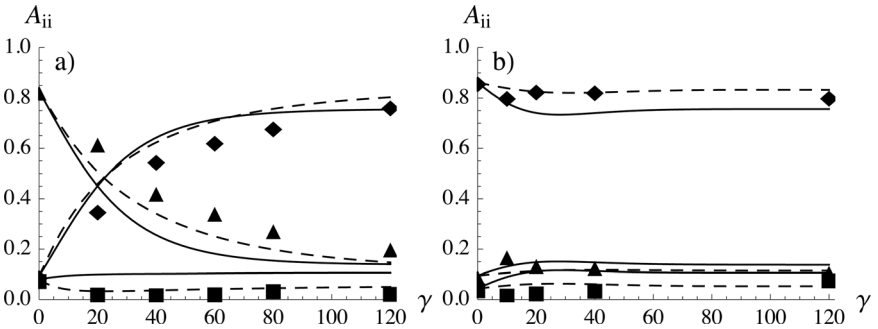

FIG. 8. (a) Comparison of orientation vs strain predictions of the Bead–Rod (solid plot) and Folgar–Tucker (dashed plot) models with experimental orientation data A_{11} (◆), A_{22} (■), and A_{33} (▲) for 30 wt.% initially neutral-direction oriented samples sheared at 1.0 s^{-1} and (b) 30 wt. % initially flow-direction oriented samples at 1.0 s^{-1}.

capturing the transient A_{11} component values. It is seen, however, that the Bead–Rod model consistently over predicts the value of the A_{22} orientation component, where as the Folgar–Tucker model more accurately predicts this component. This result was due to the quadraticlike closure approximations used for the mixed orientation moments suggested by Strautins and Latz, and described in Eqs. (18) and (19). To elaborate, it is known that the quadratic closure, in general, is less accurate in a pure shear flow [see, for example, Advani and Tucker (1987)]. Hence, we can strongly assume that the discrepancy in the A_{22} predictions is influenced by the choice of closure used in Eqs. (18) and (19). As can also be seen in Fig. 6(d), the transient orientation is only slightly dependent on shear rate (for the values used here) and appears to be governed by strain. A slight deviation from this might be seen at 4.0 s^{-1}, wherein a dip is shown in the rise of the A_{11} (and A_{33}) component at approximately 35 strain units. Both the Folgar–Tucker and Bead–Rod models predict fiber orientation to be a function of strain.

At this point, it is of interest to discuss the performance of the parameters determined using the DX samples as a unique set of material parameters for the purpose of predicting η^+ and orientation behavior of the D3 and D1 samples. Predictions for η^+ obtained for the D3 samples are shown in Fig. 7. In this case again, the BR-$\sigma_{\text{BR-mod}}$ combination out performs FT-σ_{mod}. Specifically, at both 1.0 s^{-1} and 4.0 s^{-1}, the BR-$\sigma_{\text{BR-mod}}$ combination more accurately captures the overshoot and breadth of magnitude of the overshoots. The FT-σ_{mod} combination, on the other hand, suggests a much broader and smaller overshoot, which is experimentally indicative of the rheological results obtained at 0.4 s^{-1}. At 0.4 s^{-1},

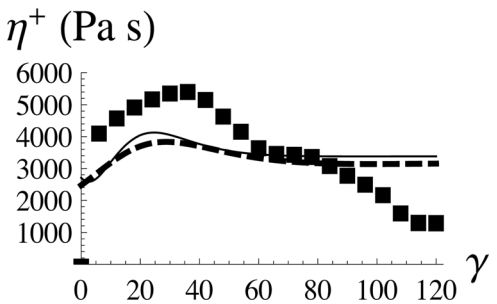

FIG. 9. Viscosity vs strain data for the 30 wt. % initially flow-direction oriented samples measured at 1.0 s^{-1} (■). Also, fit of the Bead–Rod model and (modified/proposed) stress tensor [Eq. (32)] combination (solid plot), and fit of the Folgar–Tucker model and (modified) stress tensor [Eq. (26)] combination (dashed plot).

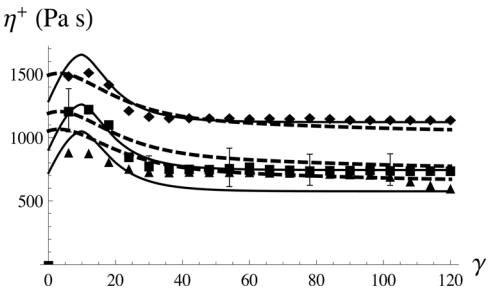

FIG. 10. Viscosity vs strain data for the 10 wt. % initially planar random oriented samples measured at 0.4 s^{-1} (◆), 1.0 s^{-1} (■), and 4.0 s^{-1} (▲). Also, fit of the Bead–Rod model and the (modified/proposed) stress tensor [Eq. (32)] combination (solid plot), and fit of the Folgar–Tucker model and (modified) stress tensor [Eq. (26)] combination (dashed plot). Error bars denote the experimental standard deviation of the data.

the FT-σ_{mod} more accurately predicts the actual magnitude of the overshoot, but both models miss the viscosity values.

The orientation predictions of both models for the D3 sample sheared at 1.0 s^{-1} are shown in Fig. 8(a). Both models slightly over predict the transient A_{11} component and under predict the A_{33} component, but certainly qualitatively capture the behavior. This statement is slightly more true for the case of the Folgar–Tucker model, which shows better orientation performance and provides results that are very close to those observed experimentally. Again, the A_{22} component is over predicted by the Bead–Rod model and was due to the quadratic nature of the closure approximations used for the mix moments

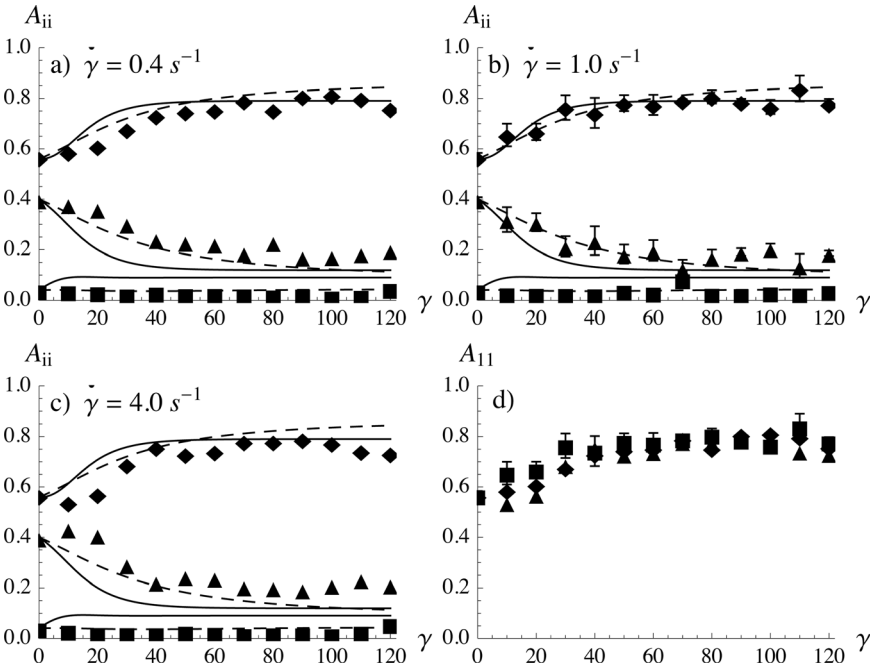

FIG. 11. Comparison of orientation vs strain predictions of the Bead–Rod (solid) and Folgar–Tucker (dashed) models with experimental orientation data A_{11} (◆), A_{22} (■), and A_{33} (▲) for 30 wt. % initially planar random oriented samples sheared at all shear rates, (a) 0.4 s^{-1}, (b), 1.0 s^{-1}, (c) 4.0 s^{-1}. (d) Comparison of experimental data A_{11} vs strain for 0.4 s^{-1} (◆), 1.0 s^{-1} (■), and 4.0 s^{-1} (▲). Error bars denote the standard deviation of the data.

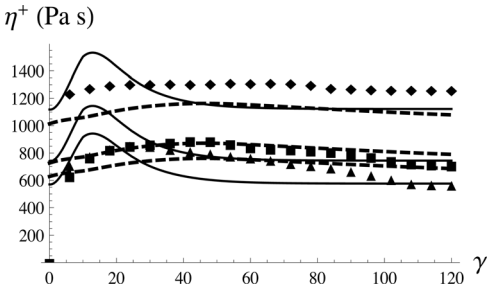

FIG. 12. Viscosity vs strain data for the 10 wt. % initially neutral-direction oriented samples measured at 0.4 s^{-1} (◆), 1.0 s^{-1} (■), and 4.0 s^{-1} (▲). Also, fit of the Bead–Rod model and (modified/proposed) stress tensor [Eq. (32)] combination (solid plot), and fit of the Folgar–Tucker model and (modified) stress tensor [Eq. (26)] combination (dashed plot).

in Eqs. (11) and (12), even though the IBOF approximation is used for $\mathbf{A}_4$, as discussed in Sec. III F.

Finally, these parameters were used to predict the rheological response for the D1 samples, Fig. 9. Both models do a very poor job at capturing the overshoot magnitude of the viscosity response, but both do capture the intermediate viscosity region. Viscosity data past 80 strain units is a phenomenon not yet understood and was not expected to be captured by any models discussed in this work. A more complete discussion of this rheology was given by Ortman *et al.* (2011). Finally, the Folgar–Tucker model more accurately captures the orientation transition, as seen in Fig. 8(b).

B. 10 wt. % materials

The same procedure was performed for the samples with a concentration of 10 wt. % fiber. The results of the fitted parameters are indicative of suspensions characterized by less fiber-fiber interactions, as compared to the 30 wt. % material, and are listed in Table I. Specifically, in both the BR-$\sigma_{\text{BR-mod}}$ and the FT-σ_{mod} combinations, lower C_I and c_2 values and higher α values were needed to fit η^+ suggesting less fiber-fiber interaction. Concerning the Bead–Rod model, less bending was predicted as a result from the lower C_I value. Again, this suggests less fiber-fiber interactions occur at lower fiber loadings, which is expected. Also, lower c_1 values and higher b values were needed to match the viscosity for both models, which we believe suggests less interfiber frictional stresses, at steady state, as

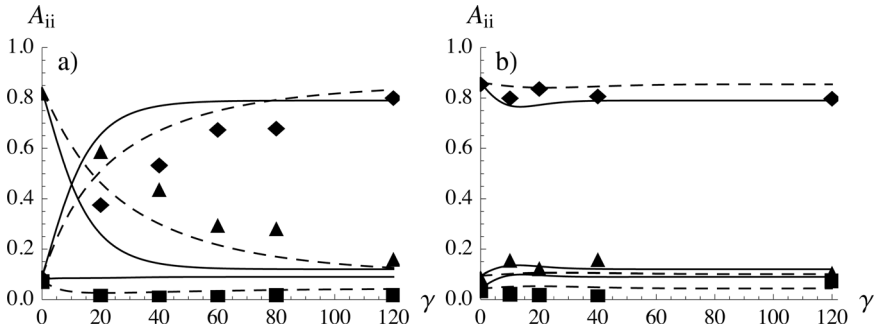

FIG. 13. (a) Comparison of orientation vs strain predictions of the Bead–Rod (solid plot) and Folgar–Tucker (dashed plot) models with experimental orientation data A_{11} (◆), A_{22} (■), and A_{33} (▲) for 10 wt. % initially neutral-direction oriented samples sheared at 1.0 s^{-1} and (b) 10 wt. % initially flow-direction oriented samples at 1.0 s^{-1}.

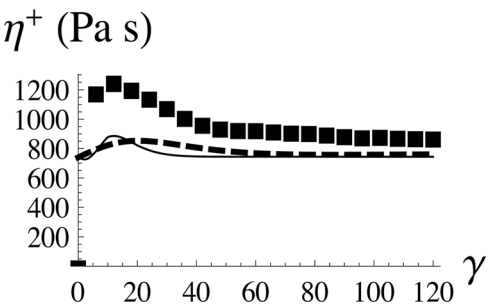

FIG. 14. Viscosity vs strain data for the 10 wt. % initially flow-direction oriented samples measured at 1.0 s^{-1} (■). Also, fit of the Bead–Rod model and (modified/proposed) stress tensor [Eq. (32)] combination (solid plot), and fit of the Folgar–Tucker model and (modified) stress tensor [Eq. (26)] combination (dashed plot).

compared to the 30 wt. % materials. To elaborate, lower c_1 values reduce the stress contribution in Eq. (27), and larger b values increase the denominator of this term and thus again reduce the stress contribution more (especially at increased shear rates).

Looking at η^+ in Fig. 10, similar fit performance is obtained in the 10 wt. % DX samples as was gained with the 30 wt. % DX samples. Specifically, the BR-$\sigma_{\text{BR-mod}}$ performs better at predicting the rheological response at the two lowest shear rates, but both models overpredict the overshoot magnitude at 4.0 s^{-1}. All model parameters are now specified and it is of interest to assess the performance of the models' orientation predictions. Referring to Figs. 11(a)–11(c), one can see the Bead–Rod slightly overpredicts the rate of orientation at 0.4 s^{-1} and 4.0 s^{-1}, whereas the Folgar–Tucker model captures this rise more accurately. Conversely, the Folgar–Tucker model slightly overpredicts the magnitude of the A_{11} component at 120 strain units, whereas the Bead—Rod model more accurately captures this value. However, in all cases, the Folgar–Tucker model performs slightly better at predicting the A_{22} and A_{33} orientation components. Finally, in Fig. 11(d), we again see that experimental orientation is again predominantly a function of deformation (strain) and does not vary much within the shear rates experimented in this research.

The performance of these parameters is now evaluated for the D3 samples, Fig. 12. As once can see, the Folgar–Tucker model more accurately predicts the shape of the response, where as the Bead–Rod model overpredicts the magnitude of the stress overshoot at each shear rate. Both models, however, due a poor job at accurately predicting the stress values at each shear rate, with the exception of the FT-σ_{mod} performance at 1.0 s^{-1}. The orientation predictions of both models for a D3 sample sheared at 1.0 s^{-1} are shown in Fig. 13(a). Both models slightly overpredict the A_{11} component and underpredict the A_{33} component values with strain, but still qualitatively capture the behavior.

Finally, these parameters were used to predict the D1 stress response, Fig. 14. The predicted rheological response greatly underpredicts the overshoot magnitude for both models explored. Additionally, both models also slightly underpredict the steady-state viscosity. Both models, however, capture the orientation dynamics, as visualized in Fig. 13(b), and in this case the Bead–Rod model predicts a slightly more accurate description of the A_{11} and A_{33} components.

V. CONCLUSIONS

In this research, we used a LGF suspension to explore an orientation model and stress tensor designed to provide a first approximation for flexible fiber systems. Specifically, we have extended the Bead–Rod orientation model to nondilute suspensions by including

isotropic rotary diffusion and also derived an appropriate stress tensor term (based on this model) that accounts for the semiflexibility of the fibers. Additionally, we showed the Lipscomb model, when coupled with the either orientation model explored, was unable to fit the transient stress data, and instead we have proposed empirical modifications to the Lipscomb model that more accurately fits this data. Specifically, in this research we explored empirical modifications to fiber stress theory that utilize weights that are functions instead of the more classical method of using constant weights.

A method for determining model parameters based on the rheology of fiber systems was demonstrated. Rheological fits showed the Bead–Rod model and associated stress theory, overall, provided a more accurate description of the stress response of the LGF systems explored. Additionally, stresses due to fiber flexibility were predicted to account for small but non-negligible bending stresses. More flexible fiber systems will be studied in the future, and it is believed that with increased flexibility the Bead–Rod model (and associated stress tensor) will be of increased value.

Finally, the orientation predictions of both models produced encouraging results in almost all cases. The Bead–Rod model and associated stress tensor, overall, produced better rheological fits and A_{11} orientation component predictions. The Folgar–Tucker model, however, produced better orientation results for the A_{33} and A_{22} in almost all the cases studied. Experimentally, the transient fiber orientation was seen to be predominately a function of strain, and only varied slightly with shear rate.

This study showed the performance of current orientation models, in simple shear flows, is very encouraging. Understanding the stress development of concentrated fiber suspensions, on the other hand, still has room for improvement. The stress responses of long fiber samples were shown to be highly dependent on the initial fiber orientation. Current stress theory does not provide a complete description for such a class of fiber suspension. The results determined in this study will be used in the future to explore the orientation development of LGFs in an injection-molded processing flow.

ACKNOWLEDGMENTS

The financial support for this work, from the National Science Foundation through Grant No. CMMI-0853537, is greatly appreciated. The authors would also like to thank SABIC for providing the materials used in this work. Additional gratitude is given to the Materials Science and Engineering department at Virginia Tech for providing polishing and microscopy facilities.

APPENDIX A: DERIVATION OF THE ISOTROPIC ROTARY DIFFUSION TERMS IN THE BEAD–ROD MODEL

First, the isotropic rotary diffusion may be introduced into the orientation balance equation. For the Bead-Rod model, this term enters as a combination of diffusion from both rods, as written in Eq. (A1), where D is the rotary diffusion coefficient.

$$D\left(\frac{\partial}{\partial \mathbf{p}^2}+\frac{\partial}{\partial \mathbf{q}^2}\right)\psi(\mathbf{p},\mathbf{q}). \tag{A1}$$

The choice of Folgar and Tucker (1984) is to equate $D = C_I\dot{\gamma}$. We now wish to form the integral moments defined in Eqs. (7)–(9) with the rotary diffusion term. For Eq. (7), the rotary diffusion term, after some manipulation [see, for example, Phelps and Tucker (2009)], becomes

$$\int\int C_I\dot{\gamma}\left[\left(\frac{\partial}{\partial \mathbf{p}^2}+\frac{\partial}{\partial \mathbf{q}^2}\right)\mathbf{pp}\right]\psi(\mathbf{p},\mathbf{q})d\mathbf{p}d\mathbf{q}. \tag{A2}$$

After expansion, the term simplifies to

$$\int\int C_I\dot{\gamma}\left(\frac{\partial}{\partial \mathbf{p}^2}\mathbf{pp}\right)\psi(\mathbf{p},\mathbf{q})d\mathbf{p}d\mathbf{q}. \tag{A3}$$

This form is exactly the same as that of the Folgar–Tucker model (1984) and upon integration over all orientation spaces become Eq. (A4), which we originally presented in Eq. (17)

$$-6C_I\dot{\gamma}\left(\mathbf{A}-\frac{1}{3}\mathbf{I}\right). \tag{A4}$$

For Eq. (8), we are interested in the mixed moment of $\mathbf{p}$ and $\mathbf{q}$ in the following manner:

$$\int\int C_I\dot{\gamma}\left(\frac{\partial}{\partial \mathbf{p}^2}+\frac{\partial}{\partial \mathbf{q}^2}\right)\psi(\mathbf{p},\mathbf{q})\mathbf{pq}d\mathbf{p}d\mathbf{q} \tag{A5}$$

$$=\int\int C_I\dot{\gamma}\frac{\partial}{\partial \mathbf{p}^2}(\mathbf{pq})\psi(\mathbf{p},\mathbf{q})d\mathbf{p}d\mathbf{q}+\int\int C_I\dot{\gamma}\frac{\partial}{\partial \mathbf{q}^2}(\mathbf{pq})\psi(\mathbf{p},\mathbf{q})d\mathbf{p}d\mathbf{q}. \tag{A6}$$

After distributing the integrand within the first integral in Eq. (A6) (and realizing that the second integral, on the average, is exactly equal to the first integral), Eq. (A6) becomes

$$=2\int\int C_I\dot{\gamma}\frac{\partial}{\partial \mathbf{p}}\left(\frac{\partial \mathbf{p}}{\partial \mathbf{p}}\mathbf{q}+\mathbf{p}\frac{\partial \mathbf{q}}{\partial \mathbf{p}}\right)\psi(\mathbf{p},\mathbf{q})d\mathbf{p}d\mathbf{q}. \tag{A7}$$

The derivative in Eq. (A7) involving the change of $\mathbf{q}$ with $\mathbf{p}$ is 0 and simplifies to become

$$=2\int\int C_I\dot{\gamma}\frac{\partial}{\partial \mathbf{p}}\left(\frac{\partial \mathbf{p}}{\partial \mathbf{p}}\mathbf{q}\right)\psi(\mathbf{p},\mathbf{q})d\mathbf{p}d\mathbf{q}, \tag{A8}$$

$$=2\int\int C_I\dot{\gamma}\frac{\partial}{\partial \mathbf{p}}[(\mathbf{I}-\mathbf{pp})\mathbf{q}]\psi(\mathbf{p},\mathbf{q})d\mathbf{p}d\mathbf{q}. \tag{A9}$$

Written in component form, the integrand of Eq. (A9) now becomes

$$=2C_I\dot{\gamma}\frac{\partial}{\partial p_l}\left[(I_{ij}-p_ip_j)q_k\right]. \tag{A10}$$

After differentiation and simplification, the term becomes

$$=2C_I\dot{\gamma}\left(-\frac{\partial p_j}{\partial p_l}p_jq_k-p_i\frac{\partial p_j}{\partial p_l}q_k\right), \tag{A11}$$

$$=2C_I\dot{\gamma}(-p_jq_k-p_iq_k). \tag{A12}$$

Upon addition, Eq. (A12) becomes

$$= -4C_I\,\dot{\gamma}\,p_j q_k. \tag{A13}$$

Upon integration this term becomes Eq. (A14), which we originally presented in Eq. (18)

$$= -4C_I\,\dot{\gamma}\int\int \mathbf{pq}\psi(\mathbf{p},\mathbf{q})d\mathbf{p}d\mathbf{q} = -4C_I\,\dot{\gamma}\,\mathbf{B}. \tag{A14}$$

Finally, for Eq. (9) we are interested in the single moment of either **p** or **q** (identical solutions will be obtained either way). Let us choose **p** for this discussion, hence the moment of interest becomes

$$C_I\,\dot{\gamma}\int\int\left(\frac{\partial}{\partial\mathbf{p}^2}+\frac{\partial}{\partial\mathbf{q}^2}\right)\mathbf{p}\psi(\mathbf{p},\mathbf{q})d\mathbf{p}d\mathbf{q}. \tag{A15}$$

Upon the first round of differentiation, noting the independence of **q** on **p**, this term becomes

$$= C_I\,\dot{\gamma}\int\int\frac{\partial}{\partial\mathbf{p}}(\mathbf{I}-\mathbf{pp})\psi(\mathbf{p},\mathbf{q})d\mathbf{p}d\mathbf{q}. \tag{A16}$$

The integrand of Eq. (A16) is therefore

$$= C_I\,\dot{\gamma}\frac{\partial}{\partial p_l}\left(I_{ij}-p_i p_j\right). \tag{A17}$$

The derivative of the identity tensor zeros out and using the chain rule of differentiation, Eq. (A17) becomes

$$= C_I\,\dot{\gamma}\left(-\frac{\partial p_j}{\partial p_l}p_j - p_i\frac{\partial p_j}{\partial p_l}\right). \tag{A18}$$

Simplification of Eq. (A18) yields

$$= -2C_I\,\dot{\gamma}\,p_j. \tag{A19}$$

Finally, upon integration this term becomes Eq. (A20), which we originally presented in Eq. (19)

$$= -2C_I\int\int\dot{\gamma}\,\mathbf{p}\psi(\mathbf{p},\mathbf{q})d\mathbf{p}d\mathbf{q} = -2C_I\,\dot{\gamma}\,\mathbf{C}. \tag{A20}$$

APPENDIX B: DERIVATION OF BENDING STRESS TERM FOR THE BEAD–ROD MODEL

We start with the restorative potential function, U(**p**,**q**), for the Bead–Rod model, see Strautins and Latz (2007).

$$U(\mathbf{p},\mathbf{q}) = \widetilde{k}(\mathbf{p}.\mathbf{q}+1). \tag{B1}$$

The force on **p**, due to the internal restorative potential therefore is

$$\mathbf{F}_p = -\frac{\partial U(\mathbf{p},\mathbf{q})}{\partial(l_B\mathbf{p})} = -\frac{\tilde{k}}{l_B}(\mathbf{I}-\mathbf{pp})\cdot\mathbf{q}, \tag{B2}$$

where the derivative of the potential function is taken on the surface of a sphere. In Eq. (B2), $\tilde{k}$ is the bending potential coefficient and its relationship to k (as seen in the Bead–Rod model) will soon be apparent. We will soon need the force on the **q** rod as well, but this term simply results in another addition of Eq. (B2). One may notice that when $\mathbf{p}=-\mathbf{q}$, the term becomes 0 and no restorative force is exists within the fiber. We now may use Kramer's stress expression to quantify the fluid stress on the suspension resulting from the forces within it. The reader is referred to the work of Doi and Edwards (1988) for a discussion of Kramer's stress expression. Including the forces of the **q** rod, we are lead to an expression for the stress tensor due to bending. The contribution of the **q** rod is exactly the same as the **p** rod (on the average) and may be accounted for by taking twice the product of Eq. (B3) and integrating it with respect to Kramer's stress expression, resulting in

$$\boldsymbol{\sigma}_{\text{bend}} = -2\left(n\frac{\tilde{k}}{l_B}\int\int \mathbf{F}_p(l_B\mathbf{p})\psi(\mathbf{p},\mathbf{q})d\mathbf{p}d\mathbf{q}\right), \tag{B3}$$

where n is the number of fibers per unit volume. Inserting Eq. (B2) into Eq. (B3), see Eq. (B4), and after some simplification, see Eq. (B5), we are left with two integrals to consider in Eq. (B6)

$$\boldsymbol{\sigma}_{\text{bend}} = 2n\tilde{k}\int\int(\mathbf{I}-\mathbf{pp})\cdot\mathbf{qp}\psi(\mathbf{p},\mathbf{q})d\mathbf{p}d\mathbf{q}, \tag{B4}$$

$$\boldsymbol{\sigma}_{\text{bend}} = 2n\tilde{k}\int\int(\mathbf{qp}-\mathbf{pp}\cdot\mathbf{qp})\psi(\mathbf{p},\mathbf{q})d\mathbf{p}d\mathbf{q}, \tag{B5}$$

$$\boldsymbol{\sigma}_{\text{bend}} = 2n\tilde{k}\left(\int\int\mathbf{qp}\psi(\mathbf{p},\mathbf{q})d\mathbf{p}d\mathbf{q} - \int\int(\mathbf{pp}\cdot\mathbf{qp})\psi(\mathbf{p},\mathbf{q})d\mathbf{p}d\mathbf{q}\right). \tag{B6}$$

At this point, we recognize the first integral as the definition of **B**, but the second integral is unknown at this point. In general, this integral requires a closure approximation to be written in terms of **A** and **B**. Such an integral also shows up in the derivation of the Bead–Rod model, see Sec. III F for a discussion, and will be handled in the manner suggested by Strautins and Latz (2007) by using a quadratic like closure for the mixed moments, as

$$\int\int(\mathbf{pp}\cdot\mathbf{qp})\psi(\mathbf{p},\mathbf{q})d\mathbf{p}d\mathbf{q} = \int\int(\mathbf{ppp}\cdot\mathbf{q})\psi(\mathbf{p},\mathbf{q})d\mathbf{p}d\mathbf{q}, \tag{B7}$$

$$\int\int(\mathbf{ppp}\cdot\mathbf{q})\psi(\mathbf{p},\mathbf{q})d\mathbf{p}d\mathbf{q} \approx \int\int(\mathbf{pp})\psi(\mathbf{p},\mathbf{q})d\mathbf{p}d\mathbf{q}\int\int(\mathbf{p}\cdot\mathbf{q})\psi(\mathbf{p},\mathbf{q})d\mathbf{p}d\mathbf{q}. \tag{B8}$$

After identifying the first integral on the right hand side of Eq. (B8) as the definition of **A**, the second integral is found to be the $tr(\mathbf{B})$. Hence, after combining the results of Eq. (B8) with Eq. (B6), the bending stress contribution becomes

$$\boldsymbol{\sigma}_{\text{bend}} = 2n\tilde{k}(\mathbf{B} - \mathbf{A}tr(\mathbf{B})). \tag{B9}$$

After inserting definitions for k [Eq. (B10)] and the coefficient of drag on a sphere [C_d in Eq. (B11)], using the theory of Doi and Edwards (1988) to quantify n [Eq. (B12)], and algebraic simplification, we are then left with the stress equation [Eq. (B13)] as originally presented in Eq. (21)

$$k = \frac{2\tilde{k}}{C_d l_B^2}, \tag{B10}$$

$$C_d = 3\pi\eta_m d, \tag{B11}$$

$$n = \frac{4\phi a_r^4}{\pi(2l_B)^3}, \tag{B12}$$

$$\boldsymbol{\sigma}_{\text{bend}} = \eta_m k \frac{3\phi a_r}{2}(\mathbf{B} - \mathbf{A}tr(\mathbf{B})). \tag{B13}$$

References

Advani, S. G., and C. L. Tucker III, "The use of tensors to describe and predict fiber orientation in short fiber composites," J. Rheol. **31**, 751–784 (1987).

Advani, S. G., and C. L. Tucker III, "Closure approximations for three-dimensional structure tensors," J. Rheol. **34**(3), 367–386 (1990).

Agarwal, N., "Transient shear flow rheology of concentrated long glass fiber suspensions in a sliding plate rheometer," Master's thesis, Virginia Polytechnic Institute and State University, Blacksburg, VA, 2009.

Batchelor, G. K., "The stress generated in a non-dilute suspension of elongated particles by pure straining motion," J. Fluid Mech. **46**, 813–829 (1971).

Bay, R. S., "Fiber orientation in injection molded composites: A comparison of theory and experiment," Ph.D. thesis, University of Illinois at Urbana-Champaign, Urbana, IL, 1991.

Chung, D. H., and T. H. Kwon, "Improved model of orthotropic closure approximation for flow induced fiber orientation," Polym. Compos. **22**(5), 636–649 (2001).

Crosby, J. M., *Long-Fiber Molding Materials* (Thermoplastic Composite Materials, Elsevier, Amsterdam, 1991), pp. 139–168.

Dinh, S. M., and R. C. Armstrong, "A rheological equation of state for semiconcentrated fiber suspensions," J. Rheol. **28**, 207–227 (1984).

Doi, M., and S. F. Edwards, *The Theory of Polymer Dynamics* (Oxford University Press, New York, 1988).

Eberle, A. P. R., D. G. Baird, and P. Wapperom, "Fiber orientation kinetics of a concentrated short glass fiber suspension in startup of simple shear flow," J. Non-Newtonian Fluid Mech. **165**(3), 110–119 (2010).

Eberle, A. P. R., D. G. Baird, P. Wapperom, and G. M. Vélez-García, "Obtaining reliable transient rheological data on concentrated short fiber suspensions using a rotational rheometer," J. Rheo. **53**, 1049–1069 (2009).

Ericksen, J. L., "Transversely isotropic fluids," Kolloid-Z. **173**, 117–122 (1960).

Folgar, F. P., and C. L. Tucker III, "Orientation behavior of fibers in concentrated suspensions," J. Reinf. Plast. Compos. **3**, 98–119 (1984).

Giacomin, A., T. Samurkas, and J. Dealy, "A novel sliding plate rheometer for molten plastics," Polym. Eng. Sci. **29**, 499–504 (1989).

Gibson, A. G., and S. Toll, "Mechanics of the squeeze flow of planar fibre suspensions," J. Non-Newtonian Fluid Mech. **82**, 1–24 (1999).

Goddard, J. D., "Tensile behavior of power-law fluids containing oriented slender fibers," J. Rheol. **22**, 615–622 (1978).

Hand, G. L., "A theory of anisotropic fluids," J. Fluid Mech. **13**, 33–46 (1962).

Hine, P. J., N. Davidson, R. A. Duckett, A. R. Clarke, and I. M. Ward, "Hydrostatically extruded glass–fiber reinforced polyoxymethylene. I. The development of fiber and matrix orientation," Polym. Compos. **17**, 720–729 (1996).

Huynh, H. M., "Improved fiber orientation predictions for injection-molded composites," Master's thesis, University of Illinois at Urbana-Champaign, 2001.

Jeffery, G. B., "The motion of ellipsoidal particles immersed in a viscous fluid," Proc. R. Soc. London Ser. A **102**, 161–179 (1922).

Joung, C. G., N. Phan-Thien, and X. J. Fan, "Direct simulation of flexible fibers," J. Non-Newtonian Fluid Mech. **99**, 1–36 (2001).

Keshtkar, M., M. C. Heuzey, and P. J. Carreau, "Rheological behavior of fiber-filled model suspensions: Effect of fiber flexibility," J. Rheo. **53**(3), 631–650 (2009).

Keshtkar, M., M.-C. Heuzey, P. J. Carreau, M. Rajabian, and C. Dubois, "Rheological properties and microstructural evolution of semi-flexible fiber suspensions under shear flow," J. Rheo. **54**(2), 197–222 (2010).

Koran, F., and J. Dealy, "A high pressure sliding plate rheometer for polymer melts," J. Rheol. **4**, 1279–1290 (1999).

Lipscomb, G. G., M. M. Denn, D. U. Hur, and D. V. Boger, "The flow of fiber suspensions in complex geometries," J. Non-Newtonian Fluid Mech. **26**, 297–325 (1988).

Ortman, K. C., N. Agarwal, A. P. R. Eberle, D. G. Baird, P. Wapperom, and A. J. Giacomin, "Transient shear flow behavior of concentrated long glass fiber suspensions in a sliding plate rheometer," J. Non-Newtonian Fluid Mech. **166**(16), 885–895 (2011).

Phelps, J., and C. L. Tucker III, "An anisotropic rotary diffusion model for fiber orientation in short- and long-fiber thermoplastics," J. Non-Newtonian Fluid Mech. **156**, 165–176 (2009).

Rajabian, M., C. Dubois, and M. Grmela, "Suspensions of semiflexible fibers in polymer fluids: Rheology and thermodynamics," Rheol. Acta **44**, 521–535 (2005).

Sepehr, M., G. Ausias, and P. Carreau, "Rheological properties of short fiber filled polypropylene in transient shear flow," J. Non-Newtonian Fluid Mech. **123**, 19–32 (2004).

Shaqfeh, E. S. G., and G. H. Fredrickson, "The hydrodynamic stress in a suspension of rods," Phys. Fluids A **2**, 7–24 (1990).

Skjetne, P., R. Ross, and D. Klingenberg, "Simulation of single fiber dynamics," J. Chem. Phys. **107**(6), 2108–2121 (1997).

Strautins, U., and A. Latz, "Flow-driven orientation dynamics of semiflexible fiber systems," Rheol. Acta **46**, 1057–1064 (2007).

Switzer, L. H. III, and D. J. Klingenberg, "Rheology of sheared flexible fiber suspensions via fiber-level simulations," J. Rheo. **47**(3), 759–778 (2003).

Vélez-García, G., "Complex flow simulation of short fiber suspended in polymer melts," Ph.D. thesis, Virginia Polytechnic Institute and State University, Blacksburg, VA, 2011.

Wang, J., J. O'Gara, and C. L. Tucker III, "An objective model for slow orientation kinetics in concentrated fiber suspensions: Theory and rheological evidence," J. Rheol. **52**(5), 1179–1200 (2008).

Yamamoto, S., and T. Matsuoka, "A method for dynamic simulation of rigid and flexible fiber in a flow field," J. Chem. Phys. **98**, 644–650 (1993).

Yamamoto, S., and T. Matsuoka, "Dynamic simulation of fiber suspensions in shear flow," J. Chem. Phys. **102**(5), 2254–2261 (1995).